Nanoscale

PAPER

View Article Online
View Journal | View Issue

Cite this: *Nanoscale*, 2023, **15**, 7352

Metal ion endogenous cycles of $CoFe_2O_{4-x}$ induced boosted photocatalytic/PMS degradation toward polycyclic aromatic hydrocarbons†

Xiaojuan Bai, *[a,b] Wei Song,[a] Xuan Ling,[a] Linlong Guo,[a] Derek Hao [c] and Xiao Zhang *[d]

The rational design of photocatalytic nanomaterials with unique structures is critical for remediating environmental problems and thus reducing ecological risks. In this work, we employed H_2 temperature-programmed reduction to modify MFe_2O_4 (M = Co, Cu, and Zn) photocatalysts for obtaining additional oxygen vacancies. After activation of PMS, naphthalene and phenanthrene degradation rates in the soil phase were increased by 3.24-fold and 1.39-fold, respectively, and 1.38-fold for naphthalene in the aqueous phase by H-$CoFe_2O_{4-x}$. The extraordinary photocatalytic activity is attributed to the oxygen vacancies on the H-$CoFe_2O_{4-x}$ surface, which promote electron transfer and thus enhance the redox cycle from Co(III)/Fe(III) to Co(II)/Fe(II). In addition, oxygen vacancies are used as electron traps to hinder the recombination of photogenerated carriers and accelerate the generation of hydroxyl and superoxide radicals. Quenching tests showed that the addition of *p*-benzoquinone resulted in the greatest decrease in the degradation rate of naphthalene (inhibition of about 85.5%), demonstrating that $O_2^{\bullet-}$ radicals are the main active species in the photocatalytic degradation of naphthalene. H-$CoFe_2O_{4-x}$ showed improved degradation performance in synergy with PMS (82.0%, k_{app} = 0.00714 min^{-1}) while maintaining excellent stability and reusability. Hence, this work provides a promising approach for the design of efficient photocatalysts to degrade persistent organic pollutants in soil and aqueous environments.

Received 30th August 2022,
Accepted 2nd March 2023

DOI: 10.1039/d3nr00727h

rsc.li/nanoscale

Introduction

With the development of global industrialization, polycyclic aromatic hydrocarbons (PAHs) have become a widespread pollutant in the environment.[1] Long-term exposure to PAHs can trigger respiratory, circulatory, and neurological damage to the liver and kidneys[2] and the International Agency for Research on Cancer has classified some PAHs as potential human carcinogens.[3] Therefore, finding an efficient and green technology to degrade PAHs has become an urgent requirement.

For efficient removal of persistent organic pollutants from water and soil, advanced oxidation processes (AOPs) based on peroxymonosulfate (PMS) have received a lot of attention.[4,5] Sulphate radicals ($SO_4^{\bullet-}$) are typical radicals for AOP remediation of soils[6] and differ from hydroxyl radicals ($^{\bullet}OH$) in the following advantages: (i) $SO_4^{\bullet-}$ can provide a greater oxidation potential (2.5–3.1 V vis. NHE) than $^{\bullet}OH$ (1.8–2.7 V *vs.* NHE).[7] (ii) Compared with $^{\bullet}OH$, $SO_4^{\bullet-}$ shows excellent selectivity and effectiveness. (iii) $SO_4^{\bullet-}$ can operate over a wide pH range. (iv) The half-life of $SO_4^{\bullet-}$ is usually longer (30–40 μs) than that of $^{\bullet}OH$ (<1 μs).[8] Transition metal catalysts have the advantages of high efficiency and ease of operation, and are one of the most feasible methods for activating PMS to produce $SO_4^{\bullet-}$.

With the further exploration of nano-photocatalytic materials,[9–12] a spinel-type metal oxide (MFe_2O_4, where M = Mn^{2+}, Co^{2+}, Ni^{2+}, Zn^{2+}, *etc.*) has attracted widespread attention. Among them, $CoFe_2O_4$, as a good semiconductor photocatalytic material, can effectively activate PMS to produce active substances.[13–16] Organic pollutants can be oxidized by oxidative species created by semiconductors, such as $^{\bullet}OH$, $O_2^{\bullet-}$, and photogenerated holes (h^+).[17–19] These highly oxidative species (h^+, $^{\bullet}OH$, and $O_2^{\bullet-}$) can degrade and even mineralize adjacent organic pollutants on the $CoFe_2O_4$ surface into CO_2, H_2O, and inorganic ions.[20,21] In previous studies, $CoFe_2O_4$ has been widely used for activating PMS to degrade 2-phenyl benzimidazole-5-sulfonic acid,[22] lomefloxacin hydrochloride,[23] sulfamethoxazole,[24] clofibrate,[25] bisphenol A,[26] *etc.*

[a]*Centre for Urban Environmental Remediation, Beijing University of Civil Engineering and Architecture, Beijing, 100044, China. E-mail: baixiaojuan@bucea.edu.cn, heixia.1986@163.com*
[b]*Beijing Energy Conservation & Sustainable Urban and Rural Development Provincial and Ministry Co-construction Collaboration Innovation Center, Beijing University of Civil Engineering and Architecture, Beijing, 100044, China*
[c]*School of Science, RMIT University, Melbourne, VIC 3000, Australia*
[d]*China Univ Petr, State Key Lab Heavy Oil Proc, Beijing 102249, P. R. China. E-mail: zhangxiao@cup.edu.cn*

† Electronic supplementary information (ESI) available. See DOI: https://doi.org/10.1039/d3nr00727h

However, due to the wide bandgap energy, the common $CoFe_2O_4$ photocatalyst has an inferior ability to separate photogenerated electron–hole pairs, which limits the degradation effect.[27] To attenuate these negative effects, researchers have inhibited the recombination of photogenerated electrons and holes and improved the photocatalytic performance of transition metal oxides by adjusting the electronic structure of cobalt ferrites.

Defect engineering is regarded as an important method in nanomaterial modification;[28–30] the electronic structure of the photocatalyst can be altered, thus significantly improving the catalytic performance.[31] As is well known, oxygen vacancies are the most common anionic defects in metallic compounds. When the oxygen vacancy is formed, the electrons near the oxygen vacancy occupy the O 2p orbital before delocalization, which promotes the electron transfer capability of the catalyst.[31,32] Oxygen vacancies can be adsorbed and continuously captured by PMS for inducing photocatalytic materials to generate $O_2^{\bullet-}$ and $^1O_2$ using dissolved oxygen. It acts as an electron transfer medium to accelerate the redox cycle from Co(III)/Fe(III) to Co(II)/Fe(II) for the synergistic degradation of organic pollutants. In addition, the localized state of the oxygen vacancy modification can extend the photoresponse and effectively trap the charge carriers.[33] Oxygen vacancy defects can be caused in a variety of ways. For example, H_2-TPR is an effective method to build surface defects, using a reducing atmosphere where a reduction reaction occurs at high temperatures to build oxygen vacancies.[34] In addition, thermal annealing under anoxic conditions is also a modulation method to generate oxygen vacancies.[35] The application in PMS activation is still limited though the oxygen-rich vacant nanoparticles have gained a lot of interest in the field of AOP. A few of the studies have used oxygen-rich cobalt ferrite activation of PMS in the aqueous and soil phases to degrade POPs.

Herein, we used the co-precipitation approach to make a series of ferrite MFe_2O_4 (M = Co, Cu, Zn) photocatalysts. Three procedures were applied to modify the samples at different temperatures to increase the oxygen vacancy content: H_2-TPR, N_2-TPD, and vacuum calcination. This work found that cobalt ferrite had the best catalytic activity for methylene blue (MB) degradation in the aqueous phase. The implications of the morphological, optical, and electrochemical properties of cobalt ferrite modified samples on photocatalytic degradation of organic contaminants were then thoroughly explored. The structure of modified cobalt ferrite and the mechanisms that increase its activity were extensively investigated by using PAHs in the aqueous and soil phases as model contaminants. This work provides new insights into natural mineral catalysts for water and soil remediation.

Experimental

Reagents and instruments

Ferric nitrate ($Fe(NO_3)_3{\cdot}9H_2O$), cobalt nitrate ($Co(NO_3)_2{\cdot}6H_2O$), zinc nitrate ($Zn(NO_3)_2{\cdot}6H_2O$), copper nitrate trihydrate ($Cu(NO_3)_2{\cdot}3H_2O$), dichloromethane (CH_2Cl_2), *tert*-butyl alcohol ($C_4H_{10}O$), edetate disodium ($[-CH_2N(CH_2CO_2Na)CH_2CO_2H]_2$), and *p*-benzoquinone ($C_6H_4O_2$) were provided by Aladdin Reagent Co., Ltd. Naphthalene ($C_{10}H_8$) was purchased from McLean Biochemical Technology Co., Ltd. Sodium hydroxide (NaOH) and ethanol (C_2H_6O) were purchased from China Phenol Reagent Co., Ltd. Methanol (CH_4O) and acetonitrile (C_2H_3N) are high-performance liquid chromatography grades, purchased from McLean Biochemical Technologies Co., Ltd.

The instruments used in the experiment are analytical balance (Gill International Trading (Shanghai) Co., Ltd); centrifuge (Shanghai Anting Scientific Instrument Factory); ultrasonic cleaner (Kunshan Ultrasonic Instrument Co., Ltd); multiple photochemical reaction instrument (Beijing Zhongjiao Jinyuan Technology Co., Ltd); Uv-vis spectrophotometer (Platinum Elmer China); ultra-performance liquid chromatography system (Shimadzu Company, Japan); scanning electron microscope, transmission electron microscope, and solid-state ultraviolet spectrophotometer (Hitachi); Fourier transform infrared spectrometer and X-ray photoelectron spectrometer (Thermo Fisher, UK); fluorescence spectrometer (JASCO); electrochemical workstation (Shanghai Chenhua Instrument Co., Ltd); high performance analog solar xenon lamp source (Beijing Pophilai Technology Co., Ltd); automatic multi-purpose adsorption instrument (Tianjin First Right Company); and tubular furnace (Hefei Kejing Material Technology Co., Ltd).

Preparation of ferrite catalysts

Analytical grade high purity chemicals and reagents were used without further purification. Preparation of MFe_2O_4 (M = Co, Zn, Cu) magnetic nanomaterials by co-precipitation.

$CoFe_2O_4$. Initially, $Co(NO_3)_2{\cdot}6H_2O$ (0.001 mol) and $Fe(NO_3)_3{\cdot}9H_2O$ (0.002 mol) were dispersed in deionized water, and kept under sonication until it was uniformly distributed. NaOH solution was added to the mixture and the pH was adjusted to 6. The solution was then stirred magnetically at 90 °C for 30 min. After the reaction, the brown-red viscous liquid was placed in a high-speed centrifuge for 4000 rpm and centrifuged for 10 min. High-speed centrifugal precipitates were washed with deionizing water. Finally, the samples were dried for 5 hours in an oven at 80 °C.

Detailed preparation processes of $ZnFe_2O_4$ and $CuFe_2O_4$ are described in the ESI (section 2.2†).

Preparation of modified ferrite catalysts

Temperature is well known to play a vital role in materials modifications. The optimum treatment temperature for the nanomaterial MFe_2O_4 (M = Co, Cu, Zn) was explored using a fully automatic multi-purpose adsorber (N_2 Temperature Programmed Desorption, TP-5080D). The tests were conducted under a dry 5% H_2/N_2 atmosphere with a 20 mL min^{-1} flow rate. The sample was purged by opening the gas cylinder during the pre-treatment phase, and after the electrical signal of the sampled values had stabilized, the first stage of temperature increase began. The sample is first warmed up to 100 °C at a rate of 10 °C min^{-1} and activated at a constant

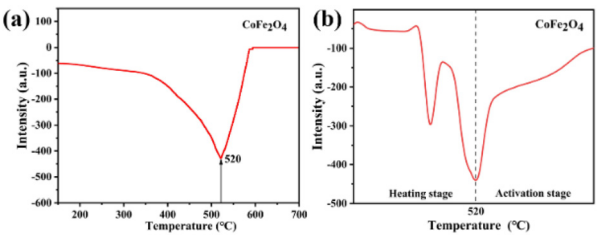

Fig. 1 (a) $CoFe_2O_4$ TPR spectrum and (b) TPR spectrum of $CoFe_2O_4$ treated at 520 °C.

temperature for 30 min to remove moisture and adsorbed gases from the surface. The temperature was then increased at a rate of 10 °C min^{-1} to 750 °C, and the electrical signals of the sampled values are displayed in Fig. 1a, b, and Fig. S2.† The temperature that corresponds to the sample's lowest value of the electrical signal is considered the optimum modification temperature, and the findings are shown in Table S1†.

A series of modified ferrite samples with different oxygen vacancy contents was obtained by annealing MFe_2O_4 (M = Co, Cu, Zn) under a 5% H_2/N_2, N_2, and vacuum atmosphere, the obtained catalysts were named H-MFe_2O_{4-x}, N-MFe_2O_{4-x}, and V-MFe_2O_{4-x}, respectively. All samples obtained were used for further characterization and applications.

H-$CoFe_2O_{4-x}$. To eliminate moisture and surface adsorbed gases from the sample, the temperature is increased to 100 °C at a rate of 10 °C min^{-1} and held at that temperature for 30 minutes. The temperature was then increased at a rate of 10 °C min^{-1} for 90 minutes from 100 °C to the optimum modification temperature (Table S1†). Fig. 1b and Fig. S2† confirm that the material starts to activate at the optimum temperature for exploration, with the potential for oxygen vacancies to arise during the activation phase due to the combination of high temperature and a reducing atmosphere.

N-$CoFe_2O_{4-x}$. To demonstrate the importance of the reducing atmosphere, throughout the trials, a dry N_2 gas stream was used. The rest of the experiment followed the same procedures as the H_2-TPR modification.

V-$CoFe_2O_{4-x}$. To investigate the effect of N_2, a vacuum atmosphere was used. $CoFe_2O_4$ was placed in a tube furnace. The vacuum environment was pumped for 30 min before the start of the ramp-up phase, the vacuum was ramped up to 400 °C, 450 °C, and 500 °C during the ramp-up phase and maintained for 90 min and the rest of the experiment was performed in the same way as the H_2-TPR modification.

The modification processes of $ZnFe_2O_4$ and $CuFe_2O_4$ are described in detail in the ESI (section 2.3†).

Characterization

All characterization means and test conditions are shown in the ESI.†

MB degradation experiment

The optimal modification temperature of the sample was evaluated by photocatalytic degradation of MB. The photocatalyst (25 mg) was mixed with a solution of MB (1×10^{-5} mol L^{-1}, 50 mL). The reaction temperature was maintained at 5 °C using a cooling water circulation system and stirred for 30 min under light-proof conditions to establish adsorption equilibrium. A xenon lamp of 250 W was used to provide visible light at an intensity of 8×10^4 Lux, and a filter (λ > 420 nm) was provided to filter out the UV fraction. Samples were taken from the solution every 20 minutes, filtered using a 0.22 μm filter membrane, and analyzed using a spectrophotometer at the maximum absorption wavelength (λ = 664 nm).

The degradation rate (%) for MB can be calculated using eqn (1):

$$\text{Degradation rate}(\%) = \frac{C_0 - C_t}{C_0} \times 100 \quad (1)$$

where C_0 (mg L^{-1}) is the initial concentration after adsorption and C_t (mg L^{-1}) is the pollutant concentration at the end of the reaction.

Aqueous-phase PAH degradation experiments

To evaluate the photodegradation of PAHs in aqueous and soil phases by synthetic samples under simulated sunlight irradiation, naphthalene was used as the target pollutant, and the temperature was controlled below 5 °C by circulating cooling water, so as to effectively avoid the volatilization of pollutants. An aqueous solution of 1 ppm naphthalene was prepared. 50 ml of naphthalene solution and 25 mg of photocatalyst were added to the photocatalytic device. The mixture was stirred for 30 min under dark conditions to reach the adsorption–desorption equilibrium. Afterward, photocatalytic degradation was carried out with a 250 W xenon lamp simulating sunlight. A cut-off filter (λ > 420 nm) was installed between the reactant and the xenon lamp to filter UV light and the light intensity was set to 8×10^4 lux. A 2 ml sample was taken at 30 min intervals and filtered through a 0.22 μm membrane for analysis.

Finally, free radical capture experiments were performed for photocatalytic degradation in naphthalene. Three trapping agents, *tert*-butyl alcohol (*t*BuOH), *p*-benzoquinone (PBQ), and disodium ethylenediaminetetraacetate (EDTA-2Na), and methanol at a concentration of 5×10^{-4} mol L^{-1} were added to the reaction solution for the photocatalytic experiments, which were consistent with the experimental procedure for the degradation of PAHs described above.

Soil phase PAH degradation experiments

The degradation of the soil phase is different from that of the aqueous phase. Garden soils were collected from Daxing district, Beijing, and collected in polyethylene sealed bags before being taken to the laboratory. Naphthalene was dissolved in methylene chloride and configured to 1 ppm of contaminated soil. 5 g of contaminated soil was taken and the ratio of soil to water was adjusted to 1 : 10 (v/v). Follow-up experiments were consistent with aqueous phase degradation.

Analytical methods

The concentration of naphthalene in the aqueous phase for photocatalytic degradation was obtained by the following method. The extracted sample was transferred into a centrifuge tube, and then the mixture was centrifuged at 4000 rpm for 10 min to achieve solid–liquid separation. After centrifugation, an appropriate amount of supernatant was filtered through a 0.22 μm filter membrane. The qualitative analysis was performed by ultra-performance liquid chromatography (UPLC)[36] using a mobile phase of methanol : water (65 : 35, v/v) at a flow rate of 1.0 mL min^{-1} and a detector wavelength of 270 nm, respectively.

Concentrations of naphthalene undergoing photocatalytic degradation in soil were obtained by the following method. The samples were transferred into centrifuge tubes, and 10 ml methanol solution was used as the extraction agent. Each sample was extracted for 30 min in an ultrasonic bath, in which the water temperature was lower than 30 °C. The mixture was then centrifuged at 4000 rpm for 10 min to achieve solid–liquid separation. The post-centrifugation operation is the same as that used for the analysis of PAHs in the aqueous phase.

The degradation efficiency of naphthalene or phenanthrene was evaluated by the ratio of the post-degradation concentration to the adsorption equilibrium concentration (C_t/C_0). The reaction rate constants were calculated using eqn (2).

$$-k_{app}t = \ln(C_t/C_0) \quad (2)$$

where k_{app} is the constant of the pseudo-first-order kinetics, t is the reaction time (min), C_0 is the concentration at which the target pollutant reaches adsorption equilibrium, and C_t is the end-of-reaction concentration.[37]

Results and discussion

Optimal temperature exploration

To evaluate the optimal modification temperature of synthetic samples, the degradation performance of the photocatalyst in MB solution was used for screening. The results showed that the optimal modification temperatures of cobalt ferrite under nitrogen, vacuum, and hydrogen atmospheres were 400 °C, 520 °C, and 520 °C, respectively. In addition, the degradation curves in Fig. 2a and b and the degradation efficiency plots in Fig. 2c, d, and Fig. S3† indicate that $CoFe_2O_4$ has the best degradation effect among the three samples under the three different modification procedures. After the creation of the oxygen defect, the change in the density of bulk $CoFe_2O_4$ is affected by the removal of the oxygen element, which causes a potential difference between metal and oxygen atoms. Coulomb forces act as a driving force for further electron migration, resulting in the migration of electrons. The valence electrons of general transition elements include the outermost electron and the d-electrons of the lower outer shell. The outer electron groupings of Co, Cu, and Zn are $3d^74s^2$, $3d^{10}4s^1$, and $3d^{10}4s^2$, respectively.[38] Cu and Zn atoms are more likely to lose

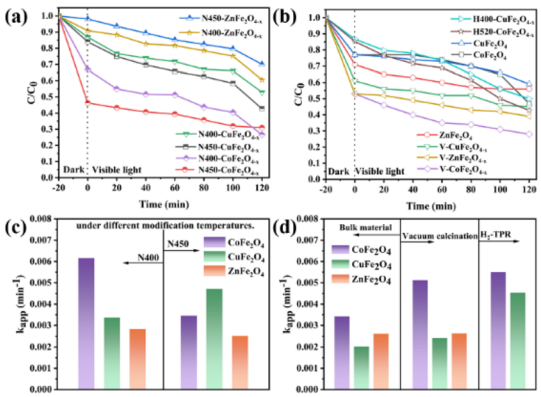

Fig. 2 MB degradation curves for (a) MFe_2O_4 (M = Co, Cu, Zn) modified by N_2-TPD at 400 and 450 °C (b) the bulk material and H_2-TPR, vacuum calcined modified material; (c) k_{app} for degradation of MB by N_2-TPD modified samples, and (d) k_{app} for degradation of MB by the bulk material and H_2-TPR, vacuum calcined modified material.

the electrons first in the outermost s-orbital, while the valence electrons in the d-orbital are completely filled and the structure is very stable. In contrast, only seven electrons in the d-orbital of the Co atom are in the unfilled state, so it is easier to lose two valence electrons in the d-orbital and become a half-filled steady-state structure. From this point of view, oxygen defects cause the change of d-orbital electron density, which further interferes with electron migration and transformation of different transition state metals, and finally results in the difference of $CoFe_2O_{4-x}$ performance compared with the other two ferrites.

Surface morphology analyses

SEM and TEM tests were performed to observe the morphological structure and characteristics of the samples. All samples show different nanoscale morphologies. $CoFe_2O_4$ consists of uniform three-dimensional nanoparticles with an average size of 2.5 μm as shown in Fig. 3a and e.[39] Moreover, $CoFe_2O_4$ particle agglomeration can be observed due to its magnetic properties.[40] The surface morphology of N-$CoFe_2O_{4-x}$ is shown in Fig. 3b and f. The particles on the surface of the sample disappear and take up a lumpy shape, due to the adsorption of nitrogen that occurs on the surface of the nanoparticles. This may cover the surface active site of N-$CoFe_2O_{4-x}$ and therefore will be detrimental to the contaminant degradation. Fig. 3c and g show that there are fine particles on the surface of V-$CoFe_2O_{4-x}$ with an average particle size of 50 nm. The morphology of H-$CoFe_2O_{4-x}$ shows a sponge-like shape with a distinct irregular porous structure and a large specific surface area. Its average particle size is 40 nm, which is the smallest among the four samples (Fig. 3d and h). It is speculated that its porous structure would be more conducive to the adsorption of pollutants and have a better catalytic effect.

To gain further insights into the samples' surface element environment and surface defects of the synthesized

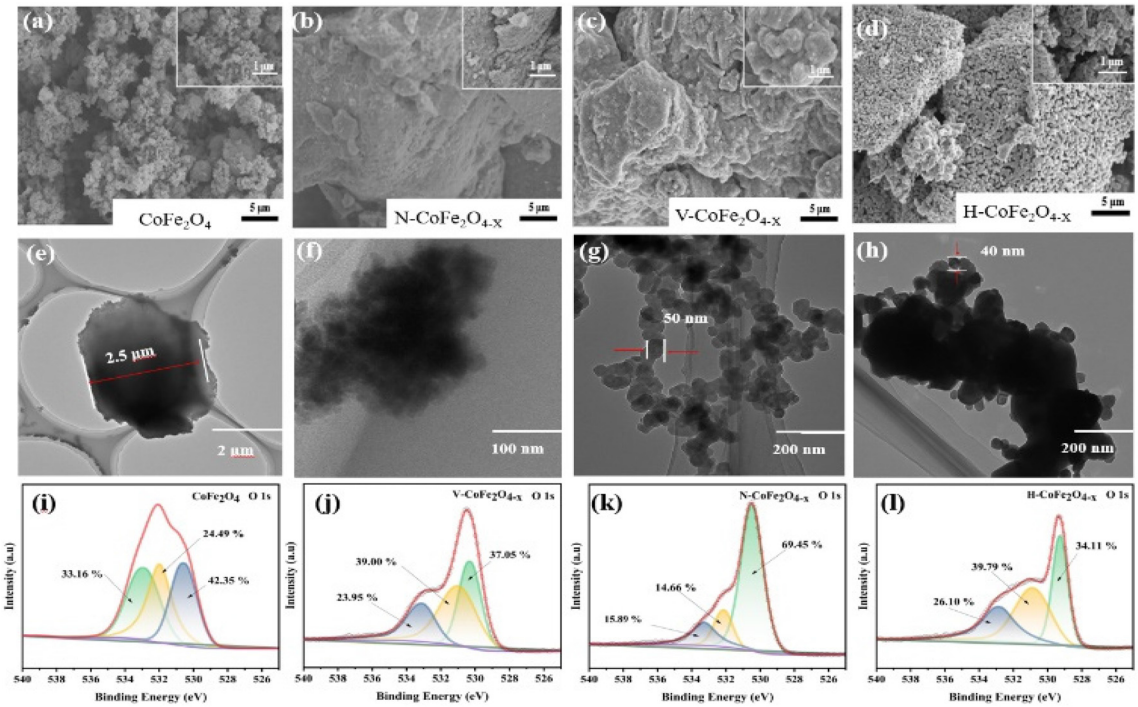

Fig. 3 SEM images of (a) $CoFe_2O_4$, (b) N-$CoFe_2O_{4-x}$, (c) V-$CoFe_2O_{4-x}$, and (d) H-$CoFe_2O_{4-x}$; TEM images of (e) $CoFe_2O_4$, (f) N-$CoFe_2O_{4-x}$, (g) V-$CoFe_2O_{4-x}$, and (h) H-$CoFe_2O_{4-x}$; and O 1s chart of (i) $CoFe_2O_4$, (j) N-$CoFe_2O_{4-x}$, (k) V-$CoFe_2O_{4-x}$, and (l) H-$CoFe_2O_{4-x}$.

$CoFe_2O_4$, N-$CoFe_2O_{4-x}$, V-$CoFe_2O_{4-x}$, and H-$CoFe_2O_{4-x}$, XPS spectra were recorded. Fig. S4a† confirms that only Fe, Co, and O elements are present in the cobalt–iron ore. In the O 1s XPS spectra of the samples (Fig. 3i–l), three peaks at 528.20, 529.57, and 530.35 eV were assigned to lattice oxygen (O_L), oxygen vacancies (O_V), and adsorbed oxygen (O_A).[41] The interaction between the surface oxygen defects and lattice oxygen has an important influence on the electron internal circulation of metal ions in the whole system. Specifically, when the oxygen vacancy is generated, the coulomb force becomes the driving force for further electron migration and transformation. In addition, the lack of lattice oxygen leads to a weak coordination structure and significant electrostatic repulsion between electrons, which increases the reducibility of the metal species, thus promoting the electron cycle between the metal ion and oxygen atom.[42] The peak area ratio of oxygen vacancies/lattice oxygen (O_V/O_L) in H-$CoFe_2O_{4-x}$ is 1.17, 2.02 times higher than that in $CoFe_2O_4$ (0.578), indicating a higher amount of oxygen vacancies in H-$CoFe_2O_{4-x}$. This is because hydrogen is a very strong reducing agent and can reduce cobalt ferrite at high temperatures.[34] Under thermal conditions, hydrogen atoms interact with lattice oxygen on the surface of $CoFe_2O_4$ to form oxygen vacancies and interstitial hydrogen. Particularly, hydrogen molecules transfer their internal electrons to surface oxygen on $CoFe_2O_4$, at high temperatures, causing oxygen atoms to undergo desorption and forming oxygen vacancies. The defect formation process is shown in eqn (3). In contrast, the N-$CoFe_2O_{4-x}$ oxygen vacancy content is only 0.211, which indicates that the formation of oxygen defects is inhibited (Table 1).[43]

$$O_L + H_2 \xrightarrow{\text{High temperature}} O_V + H_2O \quad (3)$$

Besides, Fe in $CoFe_2O_4$ has an oxidation state of +3; therefore, the higher Fe(II)/Fe(III) ratio could be a sign of a higher number of oxygen vacancies (Table 1). The Fe 2p XPS spectrum in Fig. S4(b–e)† shows that Fe $2p_{1/2}$ has two peaks at 725.25 and 711.43 eV, which proves the existence of Fe(III) in this system. A peak of Fe $2p_{3/2}$ at 713.81 eV indicates the presence of Fe(II) in the system. The satellite peaks at 716.64 eV further confirmed the existence of the Fe(III) oxidation state in $CoFe_2O_4$.[25,44,45] The calculated Fe(II)/Fe(III) ratio of H-$CoFe_2O_{4-x}$ is 0.65, 2.16 times higher than that of $CoFe_2O_4$ (0.29), in good agreement with the analysis of O 1s spectra (Table 1). The peaks of Co $2p_{3/2}$ (779.04 eV and 782.0 eV) and Co $2p_{1/2}$ (795.0 eV) are shown in Fig. S4(f–i),† together with two satellite features of 785.49 eV and 801.02 eV, respectively. The peaks at 779.04 eV and 782.0 eV indicated the presence of Co(II) oxide species, while the peak at 795.0 eV indicated the presence of Co(III) oxide species.[45] After modified treatment, the peaks of Co $2p_{3/2}$ and Co $2p_{1/2}$ of three modified samples shifted slightly to the higher binding energy region, which indicated the conversion between Co(II) and Co(III) in the catalyst. Metal cycling was attributed to the action of oxygen defects. Due to the generation of oxygen defects, an electron-rich surface is formed around the oxygen atom and dissolved oxygen gets electrons to form $O_2^{\bullet-}$ (eqn (4)). After the oxygen

Table 1 XPS results of variation in the ratio of oxygen and iron species as revealed

Samples	Atomic percentage (%)						
	Fe(II)	Fe(III)	Fe(II)/Fe(III)	O_L	O_V	O_A	O_V/O_L
$CoFe_2O_4$	22.54	77.46	0.2909	42.35	24.49	33.15	0.5782
V-$CoFe_2O_{4-x}$	24.49	75.51	0.3242	37.05	39.00	23.95	1.0526
N-$CoFe_2O_{4-x}$	27.48	72.52	0.3789	69.45	14.66	15.89	0.211
H-$CoFe_2O_{4-x}$	39.53	60.47	0.6537	34.11	39.79	26.10	1.1665

defect is produced, it promotes electron transfer due to coulomb forces and participates in the redox cycle from Co(III)/Fe(III) to Co(II)/Fe(II) to produce $^1O_2$ (eqn (5) and (6)).

$$O_2 + e^- \rightarrow O_2^{\bullet -} \quad (4)$$

$$O_2 + Fe(III) + e^- \rightarrow {}^1O_2 + Fe(II) \quad (5)$$

$$O_2 + Co(III) + e^- \rightarrow {}^1O_2 + Co(II) \quad (6)$$

As shown in Fig. 4, the XRD patterns of $CoFe_2O_4$ and H-$CoFe_2O_{4-x}$ nanoparticles showed that at 35.08°, 41.39°, 43.31°, 50.45°, 62.96°, 67.27° and 74.19°, they belong to the (220), (311), (222), (400), (422), (511) and (440) planes of the cubic spinel structure (JCPDS 22-1086).[46] The results confirmed the existence of spinel-structured $CoFe_2O_4$ nanoparticles. There is no phase transition between H-$CoFe_2O_{4-x}$ and original $CoFe_2O_4$, but the XRD peak of H-$CoFe_2O_{4-x}$ is significantly reduced. In addition, the peak (222) of H-$CoFe_2O_{4-x}$ moves toward lower 2θ values compared to the cube spinel standard position (JCPDS 22-1086). The results show that H-$CoFe_2O_{4-x}$ has a large d-spacing due to lattice distortion and lattice defects. The above phenomena are caused by the defects of the crystal structure and may be related to the formation of oxygen vacancies.[47]

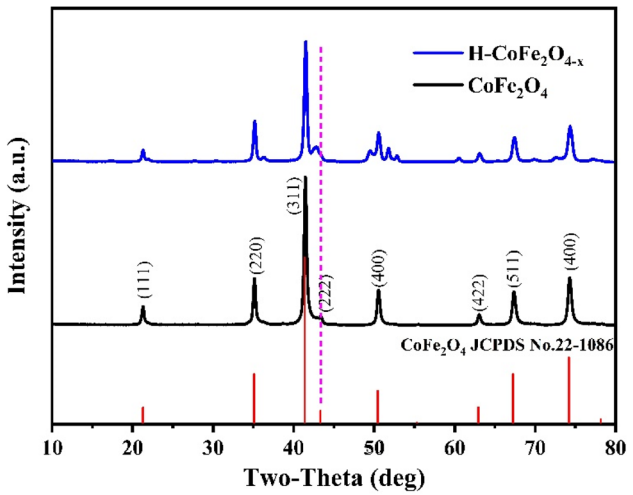

Fig. 4 XRD patterns of $CoFe_2O_4$ and H-$CoFe_2O_{4-x}$.

Optical and electrochemical characterization

The functional groups on the sample surface were investigated by infrared spectroscopy (FTIR), as shown in Fig. 5a. The FT-IR spectra of the samples at 3417, 1762, 1344, and 1049 cm^{-1} show the characteristics of nanocomposite samples. Bands at 3417 and 1762 cm^{-1} are attributed to O–H stretching vibrations and C–O stretching vibrations of the COOH $CoFe_2O_4$ groups, respectively, and bands at 1344 and 1049 cm^{-1} correspond to C–OH stretching and C–O–C stretching vibrations.[48] The high-intensity band of 600–750 cm^{-1} is caused by the inherent stretching vibrations of the tetrahedra and octahedra occupied by metal–oxygen bonds.[49] The presence of these characteristic peaks proves that the sample contains Fe(III) and Co(II). The low valent metal ions of Co(II)/Fe(II) on the catalyst surface can capture the hydroxyl groups, and in addition Co(II)/Fe(II) can serve as an active site for PMS decomposition and formation of reactive oxygen species, so the surface hydroxyl group concentration is positively correlated with the pollutant degradation rate.[50]

To determine the optical absorption characteristics and band gap energy (E_g) of the samples, UV-vis DRS analysis was performed in the range of 300 to 800 nm, and the results are shown in Fig. 5b. It can be seen that H-$CoFe_2O_{4-x}$ has a characteristic peak near 350 nm and shows light absorption ability in the UV region, indicating that H-$CoFe_2O_{4-x}$ has the ability to generate electron/hole pairs under UV light. However, compared with $CoFe_2O_4$, H-$CoFe_2O_{4-x}$ has significant absorption in both ultraviolet and visible regions, thus generating more photoinduced carriers to significantly improve its photocatalytic capacity. H-$CoFe_2O_{4-x}$ has a significant absorption effect in the visible range, which may be influenced by the black character of its sample surface.[51] The band gap energy values of the prepared samples were calculated using Kubelka–Munk theory, as shown in Fig. S5.† The band gap energy can be estimated from the tangent intercept of $(ahv)^2$ with the radiation energy. The obtained band gap energy for $CoFe_2O_4$ is 1.965 V. As for N-$CoFe_2O_{4-x}$, V-$CoFe_2O_{4-x}$, and H-$CoFe_2O_{4-x}$, the values of band gap energy are 2.097 V, 2.197 V, and 2.916 V, respectively.

Fig. 5c presents photoluminescence (PL) emission spectra of the photocatalyst monitored at an excitation wavelength of 390 nm. Of all the samples, $CoFe_2O_4$ showed the strongest fluorescence peak at 657 nm, and its fluorescence intensity was the highest, indicating that the resulting electron holes are prone to recombination. The emission intensity of the H-$CoFe_2O_{4-x}$ heterostructure is much lower than that of $CoFe_2O_4$, indicating that the recombination of photogenerated

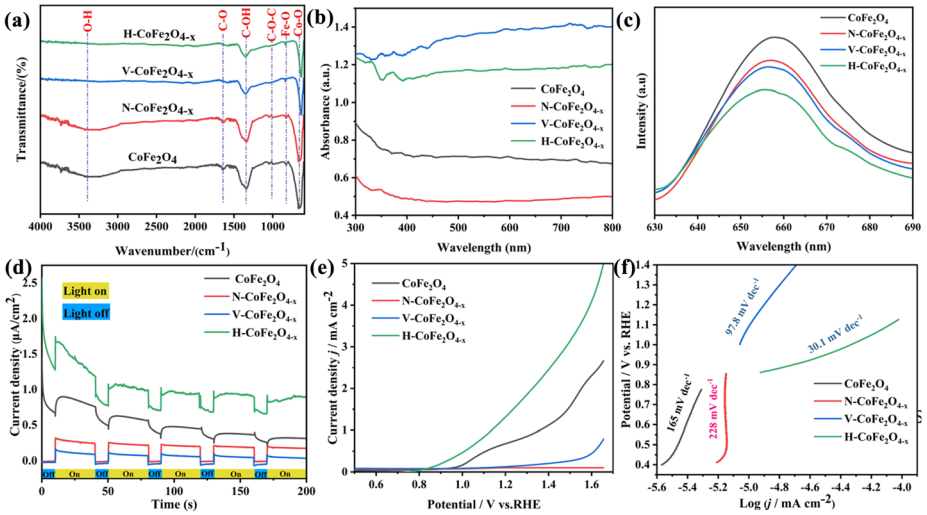

Fig. 5 (a) FT-IR, (b) diffuse reflectance UV-vis spectrum, (c) PL spectra (λ = 420 nm), (d) photocurrents under visible light irradiation, (e) linear sweep voltammetry (LSV) and (f) Tafel images of $CoFe_2O_4$, N-$CoFe_2O_{4-x}$, V-$CoFe_2O_{4-x}$, and H-$CoFe_2O_{4-x}$.

electrons and holes in the H-$CoFe_2O_{4-x}$ system is greatly inhibited.[36]

In addition, photocurrent measurements can also provide a basis for the separation rate of photogenerated carriers in heterojunctions. By analysing the relationship between photocurrent, photovoltage and optical intensity, the photocatalytic performance of the sample can be confirmed. The photocurrents of the four samples under the xenon lamp (λ > 420 nm) are shown in Fig. 5d. It is concluded that H-$CoFe_2O_{4-x}$ has the highest current density, photocurrent response value, and separation of light-generated electron–hole pairs. Linear scanning voltammetry (LSV) tests were performed on the samples and the highest cathodic currents in the curves further indicate that H-$CoFe_2O_{4-x}$ has the best electron transfer and charge separation efficiency compared with the other three samples (Fig. 5e). The Tafel slopes (Fig. 5f) of 30.1 mV dec^{-1} in H-$CoFe_2O_{4-x}$ are much lower than those in $CoFe_2O_4$ (165 mV dec^{-1}), N-$CoFe_2O_{4-x}$ (228 mV dec^{-1}) and V-$CoFe_2O_{4-x}$ (97.8 mV dec^{-1}), indicating the fastest growth in current density and the smallest change in overpotential.[52] This also indicates that the reduction of hydrogen enhances the photogenerated carrier transport rate and enables better photoelectron mobility of the sample. Based on PL spectroscopy, photocurrent, LSV diagram, and Tafel analyses, the cobalt-ferrite heterojunction formed by H-$CoFe_2O_{4-x}$ is found to be the most beneficial for carrier separation. Thus, it is more favourable for the production of active substances and promotes pollutant degradation.

To investigate the band gap energy of cobalt ferrite and modified samples, Mott–Schottky experiments were carried out. The Mott–Schottky diagram can accurately determine the type of semiconductor. A positive slope indicates that the sample has n-type properties, while a negative slope indicates p-type properties. Fig. 6(a–d) show the Mott Schottky plots obtained for the four samples at different frequencies of 1k Hz and 2k Hz, as well as the linear region of the inverse squared capacitance *versus* applied potential curves for the corresponding cobalt ferrite and its defective samples. It is shown that $CoFe_2O_4$ and H-$CoFe_2O_{4-x}$ have n-type properties, and N-$CoFe_2O_{4-x}$ and V-$CoFe_2O_{4-x}$ have p-type properties. The flat-band (FB) potentials of $CoFe_2O_4$, N-$CoFe_2O_{4-x}$, V-$CoFe_2O_{4-x}$, and H-$CoFe_2O_{4-x}$ catalys are −0.558 V, −0.279 V, 0.094 V, and −0.723 V, respectively, when the extrapolated capacitance is 0. For n-type semiconductor materials, the conversion relationship between the conduction band (E_{CB}) and E_{FB} is eqn (7); for p-type semiconductors, the conversion relationship between the valence band (E_{VB}) and E_{FB} is eqn (8).

$$E_{CB} = E_{FB} - 0.1\ V \quad (7)$$

$$E_{VB} = E_{FB} + 0.1\ V \quad (8)$$

$$E_{SCE} = E_{NHE} - 0.241\ V. \quad (9)$$

The E_{CB} values were −0.658 and −0.823 V for $CoFe_2O_4$ and H-$CoFe_2O_{4-x}$ (*vs.* SCE), and the E_{VB} values were −0.179 and 0.194 V for N-$CoFe_2O_{4-x}$ and V-$CoFe_2O_{4-x}$ (*vs.* SCE). The normal hydrogen electrode (NHE) has a certain conversion relationship with the SCE electrode, as shown by eqn (9).[53–55] The E_{NHE} values of $CoFe_2O_4$, N-$CoFe_2O_{4-x}$, V-$CoFe_2O_{4-x}$, and H-$CoFe_2O_{4-x}$ were calculated to be −0.417 V, −0.062 V, −0.435 V, and −0.582 V, respectively.

Combined with the calculation results, the band gap energy of n-type $CoFe_2O_4$ and H-$CoFe_2O_{4-x}$ and p-type N-$CoFe_2O_{4-x}$ and V-$CoFe_2O_{4-x}$ is 1.965, 2.916, 2.097, and 2.197 eV, respectively. H-$CoFe_2O_{4-x}$ can reach higher redox potentials and produce more active substances, which was due to its wider and adjustable energy band structure. Fig. 6e and f imply that the active species are $^{\bullet}OH$ and $^{\bullet}O_2^-$, thus improving the degradation of organic pollutants.

The electron transfer resistance of the synthesized samples was investigated using the electrochemical impedance spec-

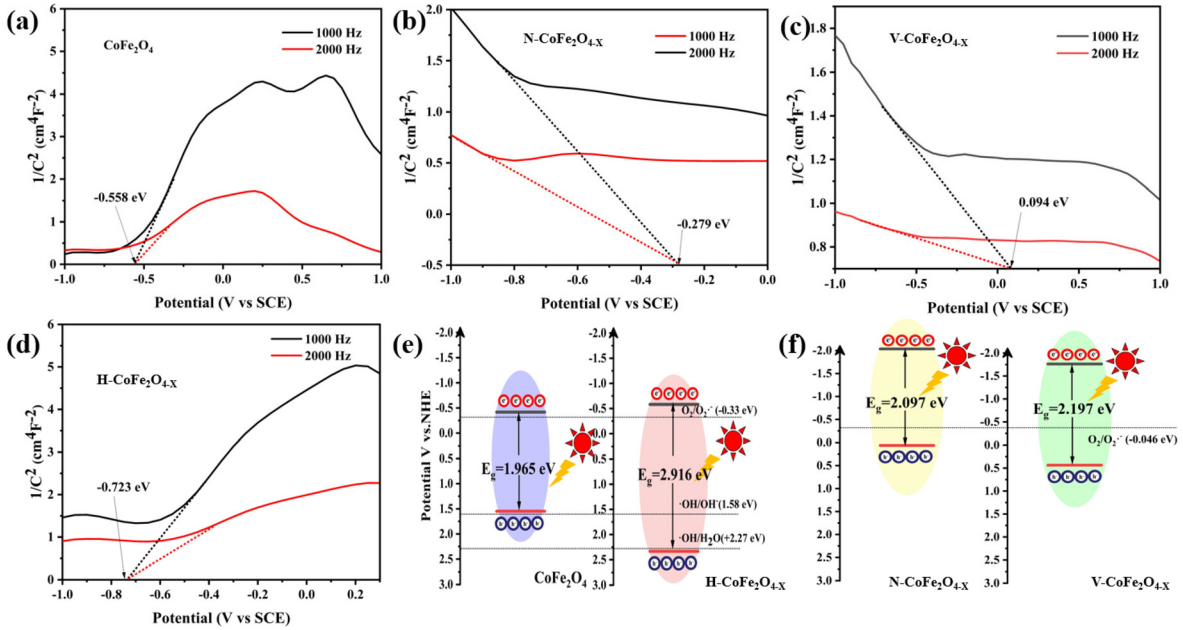

Fig. 6 Mott Schottky curves for (a) $CoFe_2O_4$, (b) N-$CoFe_2O_{4-x}$, (c) V-$CoFe_2O_{4-x}$, and (d) H-$CoFe_2O_{4-x}$; (e) energy band diagrams of n-type semiconductor photocatalytic samples $CoFe_2O_4$ and H-$CoFe_2O_{4-x}$ and (f) energy band diagrams of p-type semiconductor photocatalytic samples N-$CoFe_2O_{4-x}$ and V-$CoFe_2O_{4-x}$.

troscopy (EIS) technique. Fig. 7a depicts the Nyquist plots of the four photocatalytic samples under different conditions with the lights on and off. The high frequency region in the EIS plot is the charge transfer resistance, which mainly includes the resistance of the measured salt solution, the resistance of the experimentally made electrodes, and the contact resistance. Under the condition of turning on the lamp, the semicircles in the EIS diagram are arranged in the order of $CoFe_2O_4$ > N-$CoFe_2O_{4-x}$ > V-$CoFe_2O_{4-x}$ > H-$CoFe_2O_{4-x}$, which verifies that H-$CoFe_2O_{4-x}$ has lower charge separation and migration resistance.[56,57]

The integrated areas on the CV curves were in a descending order of H-$CoFe_2O_{4-x}$ > V-$CoFe_2O_{4-x}$ > N-$CoFe_2O_{4-x}$ > $CoFe_2O_4$. H-$CoFe_2O_{4-x}$ has the largest surface area, thus providing more active sites and thus allowing carriers to pass through (Fig. 7b) and it can be seen from the figure that the CV curve shape shows a good shuttle shape, and the H-$CoFe_2O_{4-x}$ electrode has a higher redox potential, which is favorable for the photocatalytic reaction. Fig. 7c shows the CV curves of H-$CoFe_2O_{4-x}$ at different potentials (−0.1–0.1 V, and −0.2–0.2 V). The variation of current with voltage is symmetric, indicating that H-$CoFe_2O_{4-x}$ has excellent stability, regenerative capacity, and capacitive properties. Fig. 7d shows the CV curves of H-$CoFe_2O_{4-x}$ at scan rates of 5, 10, 20, and 100 mV s^{-1}. The current response increases with increasing scan rate and remains well reproducible after 40 segments of the scan, indicating that H-$CoFe_2O_{4-x}$ has optimal rate capability and electrochemical reversibility.[58]

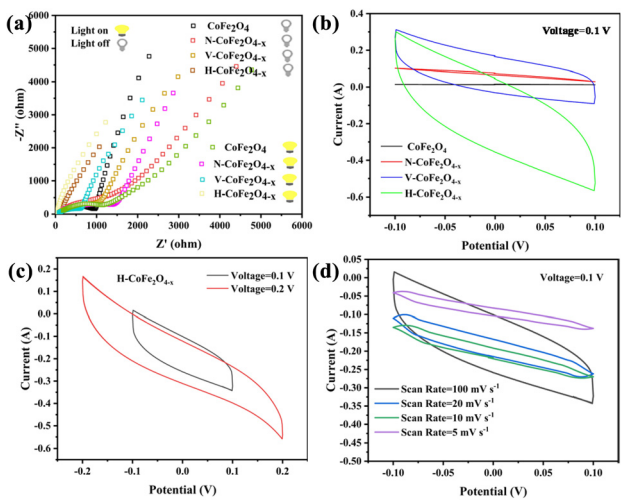

Fig. 7 (a) Electrochemical impedance spectroscopy (EIS), (b) cyclic voltammetry (CV) curves of four samples, (c) CV curves of H-$CoFe_2O_{4-x}$ at different voltages (−0.1–0.1, and −0.2–0.2 V) and (d) CV curves of H-$CoFe_2O_{4-x}$ at different scan rates (5, 10, 20, and 100 mV s^{-1}).

Assessment of photocatalysis

The microstructure, spectral properties, and photoelectrochemical properties of cobalt ferrite were analysed. The results suggest that H-$CoFe_2O_{4-x}$ has an efficient photogenerated charge separation ability and is suitable for photocatalytic degradation of pollutants. The photocatalytic activity of the samples in practical applications was assessed by the photodegradation of naphthalene and phenanthrene in the soil phase under visible light.

The plots of naphthalene degradation in soil by cobalt ferrite and modified samples are shown in Fig. 8a and b. Only 2.07% of naphthalene was degraded by $CoFe_2O_4$ within 180 min. However, the degradation rate of H-$CoFe_2O_{4-x}$ was 24.7%, which was 12 times higher compared with $CoFe_2O_4$. Fig. 8c shows the degradation efficiency, with the k_{app} in the naphthalene/H-$CoFe_2O_{4-x}$ system as 0.000913 (min^{-1}), which is 9 times higher than that of the bulk material. The degradation rate improved to 46.7% in the H-$CoFe_2O_{4-x}$/PMS system, and the k_{app} increased by 27.7 times. For the degradation of phenanthrene in PAHs, H-$CoFe_2O_{4-x}$ also showed the best degradation (Fig. 8d) with 35.1%. As shown in Fig. 8e, in the H-$CoFe_2O_{4-x}$/PMS system, the degradation rate increased to 55.2%, and k_{app} reached 0.00211 (min^{-1}), which increased by 10 times (Fig. 8f).

An unexpected finding was obtained from the degradation rate graphs in Fig. 8b and e. After 30 min of light-sensitive adsorption, the degradation rate of all samples showed a significant rebound. This is because soil is a complex system containing soil humus, soil colloids, *etc*. During the dark adsorption process, the soil's natural active agent (HA) also has a certain adsorption effect, which temporarily reduces the concentration of organic pollution.[59] When visible light was provided, the desorption of NAP in the soil was enhanced and the concentration gradually rebounded.

The photocatalytic degradation of naphthalene at 1 ppm in the aqueous phase was carried out in the presence of 25 mg of catalyst. It can be seen from Fig. 9a that H-$CoFe_2O_{4-x}$ has the best degradation effect within 180 min, and the degradation rate can reach about 60%, which is 23% higher than that of $CoFe_2O_4$. The k_{app} value was 0.00289 min^{-1}, 3.5 times that of the bulk material (Fig. 9c and Fig. S6†). After that, the photocatalyst/PMS system was constructed by adding PMS at a concentration of 1 mmol L^{-1} to the aqueous phase, which also degraded 1 ppm aqueous naphthalene solution. The degradation curves within 180 min are shown in Fig. 9b, and the degradation effect was significantly improved. Among them, H-$CoFe_2O_{4-x}$ had the best degradation effect in cooperation with PMS (82.0%, k_{app} = 0.00714 min^{-1}), and it can be concluded that H-$CoFe_2O_{4-x}$ can effectively activate PMS to generate active species and promote the degradation of pollutants.[60] In practical applications, recyclability and stability are important indicators to evaluate the catalyst performance. For this purpose, the degree of pollutant mineralization was evaluated by four consecutive cycles of the H-$CoFe_2O_{4-x}$/PMS system for the degradation of 1 ppm naphthalene. As shown in Fig. 9d and Fig. S7,† no significant degradation was observed after four repeated runs, and the high catalytic performance (>73.6%) was still maintained. In addition, H-$CoFe_2O_{4-x}$ has good magnetic properties (Fig. S8†) and can be used as a recyclable catalyst with high application potential and good economic benefits.

Cyclic voltammetry was used to analyse the H-$CoFe_2O_{4-x}$ after cyclic degradation (Fig. 9e). The sample was subjected to an electric potential (−0.1–0.1 V) and different sweep rates (5, 10, 20, and 100 mV s^{-1}). The results were essentially the same as for the samples before cyclic degradation. Furthermore, the stability of of H-$CoFe_2O_{4-x}$ can be analyzed by the EIS spectra before and after cyclic degradation (Fig. 9f). The intersection

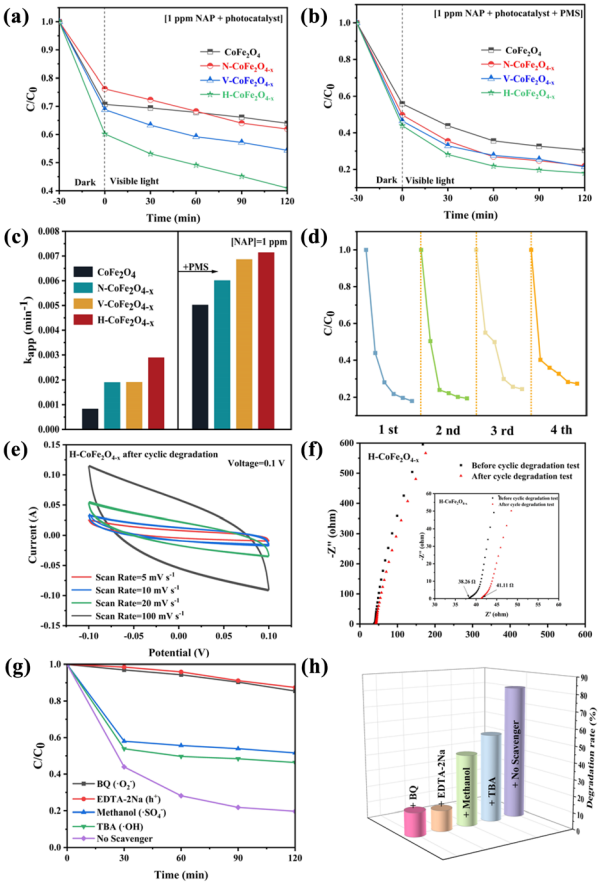

Fig. 9 (a) Naphthalene degradation curve ([NAP] = 1 ppm), (b) synergistic PMS degradation curve, (c) k_{app} value, (d) naphthalene degradation cycling experiment ([NAP] = 1 ppm), (e) CV curves of H-$CoFe_2O_{4-x}$ after cyclic degradation, (f) EIS profile of H-$CoFe_2O_{4-x}$ after cyclic degradation (illustration is an EIS enlarged view), (g) effect of free radical scavengers on naphthalene degradation ([NAP] = 1 ppm) and (h) degradation rate by the action of free radical scavengers.

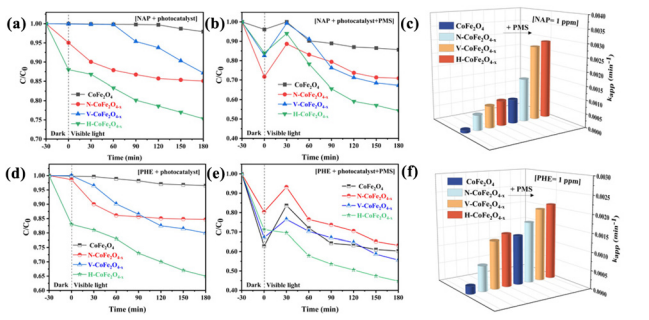

Fig. 8 Degraded naphthalene in the soil phase: (a) degradation curve ([NAP] = 1 ppm), (b) synergistic PMS degradation curve, (c) k_{app} value; degraded phenanthrene in the soil phase, (d) degradation curve ([PHE] = 1 ppm), (e) synergistic PMS degradation curve, and (f) k_{app} value.

of the EIS and the real axis indicates the solution resistance (R_s) of the electrode,[61] and the values of R_s before and after cyclic degradation of H-$CoFe_2O_{4-x}$ are 38.26 Ω and 41.11 Ω, respectively, with little change in resistance, indicating that the sample has high stability.

Photocatalytic mechanism

The quenching experiment was carried out to determine the type of free radical generated. *tert*-Butanol (TBA), disodium ethylenediaminetetraacetate (EDTA-2Na) and *p*-benzoquinone (BQ) were used to quench the radicals against $^{\bullet}OH$, h^+ and $^{\bullet}O_2^-$, respectively, and $SO_4^{\bullet-}$ and $^{\bullet}OH$ radicals were quenched by methanol (Fig. 9g). As can be seen from Fig. 9h, the degradation rate of naphthalene solution with the addition of BQ and EDTA-2Na was the lowest, indicating that a large amount of $^{\bullet}O_2^-$ and h^+ was captured. Therefore, $^{\bullet}O_2^-$ and h^+ radicals play an important role in the H-$CoFe_2O_{4-x}$/PMS system. Meanwhile, $^{\bullet}OH$ and $SO_4^{\bullet-}$ play an auxiliary effect in the degradation process of organic pollutants.

Structural changes of the samples after modification and the mechanism diagram of degradation of PAHs by activated PMS with H-$CoFe_2O_{4-x}$ are shown in Fig. 10. The high temperature treatment of $CoFe_2O_4$ under a hydrogen atmosphere resulted in a porous structure, which promoted the adsorption of pollutants. Hydrogen reacts with oxygen in the sample to form H_2O, and oxygen vacancies appear on the surface of the material. H-$CoFe_2O_{4-x}$ undergoes charge separation and generates electrons and holes under visible light irradiation (eqn (10)). Electrons can then combine with dissolved oxygen to produce $O_2^{\bullet-}$ (eqn (11)). The process of oxidation of water molecules to generate $^{\bullet}OH$ radicals is mainly through the transfer of photogenerated h^+ to water molecules and the breaking of O–H bonds to generate $^{\bullet}OH$ (eqn (12)).

After the oxygen defect is produced, the change of oxygen atomic density is affected by the removal of the oxygen element, resulting in the potential difference with the metal. The coulomb force acts as the driving force for further electron migration, promoting electron transfer and enhancing the redox cycle (eqn (13)) from Co(III)/Fe(III) to Co(II)/Fe(II), thus promoting the formation of $^1O_2$ and $O_2^{\bullet-}$. Due to the existence of oxygen vacancies on the surface of H-$CoFe_2O_{4-x}$, the electronic properties of metal sites can be effectively regulated to form an electron-rich surface. In addition, more active sites can be provided as PMS activation centers to generate $^{\bullet}OH$ and $SO_4^{\bullet-}$ for efficient degradation of organic pollutants (eqn (14)). Finally, combined with quenching experiments, $O_2^{\bullet-}$ and h^+ radicals play an important role in the H-$CoFe_2O_{4-x}$/PMS system. At the same time, $^{\bullet}OH$ and $SO_4^{\bullet-}$ play auxiliary roles in the degradation of organic pollutants (eqn (15)).

$$\text{H-}CoFe_2O_{4-x} + h\nu \rightarrow \text{H-}CoFe_2O_{4-x}(e) + \text{H-}CoFe_2O_{4-x}(h) \quad (10)$$

$$\text{H-}CoFe_2O_{4-x}(e) + O_2 \rightarrow \text{H-}CoFe_2O_{4-x} + O_2^{\bullet-} \quad (11)$$

$$\text{H-}CoFe_2O_{4-x}(h) + OH^- \rightarrow \text{H-}CoFe_2O_{4-x} + {}^{\bullet}OH \quad (12)$$

$$O_2 + \text{Fe(III)/Co(III)} + 2e^- \rightarrow O_2^{\bullet-} + \text{Fe(II)/Co(II)} \quad (13)$$

$$\text{Fe(II)/Co(II)} + \text{PMS} \rightarrow \text{Fe(III)/Co(III)} + SO_4^{\bullet-} + {}^{\bullet}OH \quad (14)$$

$$O_2^{\bullet-}(h^+, {}^{\bullet}OH, {}^1O_2) + \text{naphthalene} \rightarrow CO_2 + H_2O \quad (15)$$

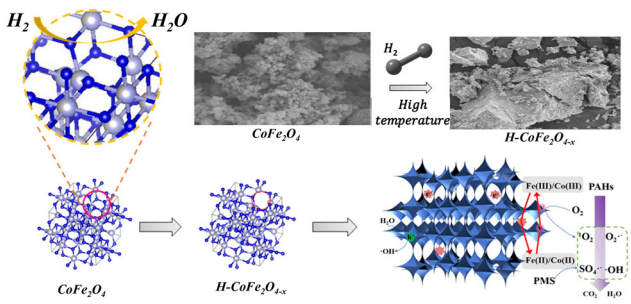

Fig. 10 Structural changes of the samples after modification and the mechanism diagram of degradation of PAHs by activated PMS with H-$CoFe_2O_{4-x}$.

Conclusions

In summary, we have synthesized H-$CoFe_2O_{4-x}$ containing suitable oxygen vacancies by using H_2-TPR to meet the needs of aqueous and soil phase pollution remediation. H-$CoFe_2O_{4-x}$ coupled with a PMS activation system exhibited excellent photocatalytic activity. The degradation rates of naphthalene and phenanthrene in the soil phase increased by 3.24-fold and 1.39-fold, respectively, and 1.38-fold for naphthalene in the aqueous phase by H-$CoFe_2O_{4-x}$. Electrochemical methods were used to confirm that the oxygen vacancies on the H-$CoFe_2O_{4-x}$ surface accelerate electron transfer. Meanwhile, it enhances the redox cycle from Co(III)/Fe(III) to Co(II)/Fe(II), and then promotes the formation of $^{\bullet}O_2^-$. In the H-$CoFe_2O_{4-x}$/PMS system, the radical scavenging experiments confirmed that $O_2^{\bullet-}$ and h^+ were the main reactive radicals in the degradation of PAHs. In particular, the optimized H-$CoFe_2O_{4-x}$ photocatalyst was magnetic and easy to recover, and had superior cycling stability. This study provides a promising remediation method for designing efficient photocatalysts to improve the photocatalytic performance of PAHs in the aqueous phase and soil.

Author contributions

Xiaojuan Bai: conceptualization, writing – review, supervision and resources. Wei Song: experiment, conceptualization, validation, data curation and writing. Xuan Ling: experiment and writing – review. Linlong Guo: conceptualization and resources. Derek Hao: supervision. Xiao Zhang: supervision.

Conflicts of interest

There are no conflicts to declare.

Acknowledgements

This work was partly supported by the National Key R&D Program of China (2020YFC1808805), National Natural Science Foundation of China (22276011 and 21607034), Beijing Natural Science Foundation (8192011), Science and Technology General Project of Beijing Municipal Education Commission (KM202010016006), and the Pyramid Talent Training Project of Beijing University of Civil Engineering and Architecture (JDYC20200313).

References

1 Z. Liu, Y. Fei, H. Shi, L. Mo and J. Qi, Prediction of high-risk areas of soil heavy metal pollution with multiple factors on a large scale in industrial agglomeration areas, *Sci. Total Environ.*, 2022, **808**, 151874.

2 S. Khadhar, T. Higashi, H. Hamdi, S. Matsuyama and A. Charef, Distribution of 16 EPA-priority polycyclic aromatic hydrocarbons (PAHs) in sludges collected from nine Tunisian wastewater treatment plants, *J. Hazard. Mater.*, 2010, **183**, 98–102.

3 O. Idowu, K. T. Semple, K. Ramadass, W. O'Connor, P. Hansbro and P. Thavamani, Beyond the obvious: Environmental health implications of polar polycyclic aromatic hydrocarbons, *Environ. Int.*, 2019, **123**, 543–557.

4 Y. Peng, H. Tang, B. Yao, X. Gao, X. Yang and Y. Zhou, Activation of peroxymonosulfate (PMS) by spinel ferrite and their composites in degradation of organic pollutants: A Review, *Chem. Eng. J.*, 2021, **414**, 128800.

5 X. Zhou, A. Jawad, M. Luo, C. Luo, T. Zhang, H. Wang, J. Wang, S. Wang, Z. Chen and Z. Chen, Regulating activation pathway of Cu/persulfate through the incorporation of unreducible metal oxides: Pivotal role of surface oxygen vacancies, *Appl. Catal., B*, 2021, **286**, 119914.

6 M. Mahdi Ahmed, S. Barbati, P. Doumenq and S. Chiron, Sulfate radical anion oxidation of diclofenac and sulfamethoxazole for water decontamination, *Chem. Eng. J.*, 2012, **197**, 440–447.

7 L. Wu, Q. Zhang, J. Hong, Z. Dong and J. Wang, Degradation of bisphenol A by persulfate activation via oxygen vacancy-rich $CoFe_2O_{4-x}$, *Chemosphere*, 2019, **221**, 412–422.

8 H. Chen, Y. Xu, K. Zhu and H. Zhang, Understanding oxygen-deficient $La_2CuO_{4-\delta}$ perovskite activated peroxymonosulfate for bisphenol A degradation: The role of localized electron within oxygen vacancy, *Appl. Catal., B*, 2021, **284**, 119732.

9 Y. Dai and Y. Xiong, Control of selectivity in organic synthesis via heterogeneous photocatalysis under visible light, *Nano Res. Energy*, 2022, **1**, e9120006.

10 D. Hao, Y. Liu, S. Gao, H. Arandiyan, X. Bai, Q. Kong, W. Wei, P. K. Shen and B.-J. Ni, Emerging artificial nitrogen cycle processes through novel electrochemical and photochemical synthesis, *Mater. Today*, 2021, **46**, 212–233.

11 D. Hao, J. Ren, Y. Wang, H. Arandiyan, M. Garbrecht, X. Bai, H. K. Shon, W. Wei and B.-J. Ni, A Green Synthesis of Ru Modified g-C_3N_4 Nanosheets for Enhanced Photocatalytic Ammonia Synthesis, *Energy Mater. Adv.*, 2021, **2021**, 9761263.

12 Z. Han, M. Lv, X. Shi, G. Li, J. Zhao and X. Zhao, Regulating the Electronic Structure of Fe^{3+}-Doped $BiOCl_xI_{1-x}$ Solid Solution by an Amidoxime-Functionalized Fibrous Support for Efficient Photocatalysis, *Adv. Fiber Mater.*, 2022, **5**, 266–281.

13 E. Skliri, J. Miao, J. Xie, G. Liu, T. Salim, B. Liu, Q. Zhang and G. S. Armatas, Assembly and photochemical properties of mesoporous networks of spinel ferrite nanoparticles for environmental photocatalytic remediation, *Appl. Catal., B*, 2018, **227**, 330–339.

14 W. Kong, L. Huang, X. Quan and G. L. Puma, Synergistic induced charge transfer switch by oxygen vacancy and pyrrolic nitrogen in $MnFe_2O_4$/g-C_3N_4 heterojunctions for efficient transformation of bicarbonate to acetate in photo-assisted MES, *Appl. Catal., B*, 2022, **307**, 121214.

15 P. Mishra, L. Acharya and K. Parida, A comparison study between novel ternary retrieval $NiFe_2O_4$@P-doped g-C_3N_4 and Fe_3O_4@P-doped g-C_3N_4 nanocomposite in the field of photocatalysis, H_2 energy production and super capacitive property, *Mater. Today*, 2021, **35**, 281–288.

16 Y. Zhou, W. Jiao, Y. Xie, F. He, Y. Ling, Q. Yang, J. Zhao, H. Ye and Y. Hou, Enhanced photocatalytic CO_2-reduction activity to form CO and CH_4 on S-scheme heterostructured $ZnFe_2O_4/Bi_2MoO_6$ photocatalyst, *J. Colloid Interface Sci.*, 2022, **608**, 2213–2223.

17 Y. Li, X. Wang, J. Gong, Y. Xie, X. Wu and G. Zhang, Graphene-Based Nanocomposites for Efficient Photocatalytic Hydrogen Evolution: Insight into the Interface toward Separation of Photogenerated Charges, *ACS Appl. Mater. Interfaces*, 2018, **10**, 43760–43767.

18 X. Liang, G. Wang, X. Dong, G. Wang, H. Ma and X. Zhang, Graphitic Carbon Nitride with Carbon Vacancies for Photocatalytic Degradation of Bisphenol A, *ACS Appl. Nano Mater.*, 2018, **2**, 517–524.

19 I. Mukherjee, V. Cilamkoti and R. K. Dutta, Sunlight-Driven Photocatalytic Degradation of Ciprofloxacin by Carbon Dots Embedded in ZnO Nanostructures, *ACS Appl. Nano Mater.*, 2021, **4**, 7686–7697.

20 D. Li, Q. Zhu, C. Han, Y. Yang, W. Jiang and Z. Zhang, Photocatalytic degradation of recalcitrant organic pollutants in water using a novel cylindrical multi-column photoreactor packed with TiO_2-coated silica gel beads, *J. Hazard. Mater.*, 2015, **285**, 398–408.

21 G. Xian, S. Kong, Q. Li, G. Zhang, N. Zhou, H. Du and L. Niu, Synthesis of Spinel Ferrite MFe_2O_4 (M = Co, Cu, Mn, and Zn) for Persulfate Activation to Remove Aqueous Organics: Effects of M-Site Metal and Synthetic Method, *Front. Chem.*, 2020, **8**, 177.

22 A. Al-Anazi, W. H. Abdelraheem, C. Han, M. N. Nadagouda, L. Sygellou, M. K. Arfanis, P. Falaras, V. K. Sharma and D. D. Dionysiou, Cobalt ferrite nanoparticles with con-

trolled composition-peroxymonosulfate mediated degradation of 2-phenylbenzimidazole-5-sulfonic acid, *Appl. Catal., B*, 2018, **221**, 266–279.

23 Y. You, Z. Shi, Y. Li, Z. Zhao, B. He and X. Cheng, Magnetic cobalt ferrite biochar composite as peroxymonosulfate activator for removal of lomefloxacin hydrochloride, *Sep. Purif. Technol.*, 2021, **272**, 118889.

24 D. Oh, C.-S. Lee, Y.-G. Kang and Y.-S. Chang, Hydroxylamine-assisted peroxymonosulfate activation using cobalt ferrite for sulfamethoxazole degradation, *Chem. Eng. J.*, 2020, **386**, 123751.

25 C. Cai, X. Duan, X. Xie, S. Kang, C. Liao, J. Dong, Y. Liu, S. Xiang and D. D. Dionysiou, Efficient degradation of clofibric acid by heterogeneous catalytic ozonation using $CoFe_2O_4$ catalyst in water, *J. Hazard. Mater.*, 2021, **410**, 124604.

26 X. Long, C. Feng, D. Ding, N. Chen, S. Yang, H. Chen, X. Wang and R. Chen, Oxygen vacancies-enriched $CoFe_2O_4$ for peroxymonosulfate activation: The reactivity between radical-nonradical coupling way and bisphenol A, *J. Hazard. Mater.*, 2021, **418**, 126357.

27 S. Swathi, R. Yuvakkumar, P. S. Kumar, G. Ravi and D. Velauthapillai, Annealing temperature effect on cobalt ferrite nanoparticles for photocatalytic degradation, *Chemosphere*, 2021, **281**, 130903.

28 M. L. Lizhen Liu, F. Chen and H. Huang, Recent Advances on Single–Atom Catalysts for CO_2 Reduction, *Small Struct.*, 2023, **4**, 2200188.

29 F. Chen, Y. Zhang and H. Huang, Layered photocatalytic nanomaterials for environmental applications, *Chin. Chem. Lett.*, 2023, **34**, 107523.

30 F. Chen, Z. Ma, L. Ye, T. Ma, T. Zhang, Y. Zhang and H. Huang, Macroscopic Spontaneous Polarization and Surface Oxygen Vacancies Collaboratively Boosting CO(2) Photoreduction on BiOIO(3) Single Crystals, *Adv. Mater.*, 2020, **32**, e1908350.

31 Y. Zhao, C. Chang, F. Teng, Y. Zhao, G. Chen, R. Shi, G. I. N. Waterhouse, W. Huang and T. Zhang, Defect-Engineered Ultrathin δ-MnO2 Nanosheet Arrays as Bifunctional Electrodes for Efficient Overall Water Splitting, *Adv. Energy Mater.*, 2017, **7**, 1700005.

32 C. Hu, S. Tu, N. Tian, T. Ma, Y. Zhang and H. Huang, Photocatalysis Enhanced by External Fields, *Angew. Chem., Int. Ed.*, 2021, **60**, 16309–16328.

33 H. Zhang, C. Li, L. Lyu and C. Hu, Surface oxygen vacancy inducing peroxymonosulfate activation through electron donation of pollutants over cobalt-zinc ferrite for water purification, *Appl. Catal., B*, 2020, **270**, 118874.

34 Y. Jian, M. Tian, C. He, J. Xiong, Z. Jiang, H. Jin, L. Zheng, R. Albilali and J.-W. Shi, Efficient propane low-temperature destruction by Co_3O_4 crystal facets engineering: Unveiling the decisive role of lattice and oxygen defects and surface acid-base pairs, *Appl. Catal., B*, 2021, **283**, 119657.

35 H. Wang, C. Tang, W. Yang, J. Zhao, L. Liu, J. Mu, Y. Zhang and C. Zeng, Recrystallization behavior, oxygen vacancy and photoluminescence performance of sputter-deposited Ga_2O_3 films via high-vacuum in situ annealing, *Ceram. Int.*, 2022, **48**, 3481–3488.

36 Y. Fu, H. Chen, X. Sun and X. Wang, Combination of cobalt ferrite and graphene: High-performance and recyclable visible-light photocatalysis, *Appl. Catal., B*, 2012, **111–112**, 280–287.

37 L. Cao, D. Chen, W. Li and R. A. Caruso, Hierarchically porous titania networks with tunable anatase:rutile ratios and their enhanced photocatalytic activities, *ACS Appl. Mater. Interfaces*, 2014, **6**, 13129–13137.

38 M. Hasegawa and T. Yagi, Systematic study of formation and crystal structure of 3d-transition metal nitrides synthesized in a supercritical nitrogen fluid under 10 GPa and 1800 K using diamond anvil cell and YAG laser heating, *J. Alloys Compd.*, 2005, **403**, 131–142.

39 J. Liu, R. Meng, J. Li, P. Jian, L. Wang and R. Jian, Achieving high-performance for catalytic epoxidation of styrene with uniform magnetically separable $CoFe_2O_4$ nanoparticles, *Appl. Catal., B*, 2019, **254**, 214–222.

40 J. Deng, Y. Shao, N. Gao, C. Tan, S. Zhou and X. Hu, $CoFe_2O_4$ magnetic nanoparticles as a highly active heterogeneous catalyst of oxone for the degradation of diclofenac in water, *J. Hazard. Mater.*, 2013, **262**, 836–844.

41 Y. Xu, L. Zheng, C. Yang, W. Zheng, X. Liu and J. Zhang, Oxygen Vacancies Enabled Porous SnO_2 Thin Films for Highly Sensitive Detection of Triethylamine at Room Temperature, *ACS Appl. Mater. Interfaces*, 2020, **12**, 20704–20713.

42 T. Cong Khiem, D. Dinh Tuan, E. Kwon, N. Nhat Huy, W.-D. Oh, W.-H. Chen and K.-Y. A. Lin, Degradation of dihydroxybenzophenone through monopersulfate activation over nanostructured cobalt ferrites with various morphologies: A comparative study, *Chem. Eng. J.*, 2022, **450**, 137798.

43 J. Yang, S. Hu, Y. Fang, S. Hoang, L. Li, W. Yang, Z. Liang, J. Wu, J. Hu, W. Xiao, C. Pan, Z. Luo, J. Ding, L. Zhang and Y. Guo, Oxygen Vacancy Promoted O_2 Activation over Perovskite Oxide for Low-Temperature CO Oxidation, *ACS Catal.*, 2019, **9**, 9751–9763.

44 Y. Bao, T.-T. Lim, R. Wang, R. D. Webster and X. Hu, Urea-assisted one-step synthesis of cobalt ferrite impregnated ceramic membrane for sulfamethoxazole degradation via peroxymonosulfate activation, *Chem. Eng. J.*, 2018, **343**, 737–747.

45 M. Xu, J. Li, Y. Yan, X. Zhao, J. Yan, Y. Zhang, B. Lai, X. Chen and L. Song, Catalytic degradation of sulfamethoxazole through peroxymonosulfate activated with expanded graphite loaded $CoFe_2O_4$ particles, *Chem. Eng. J.*, 2019, **369**, 403–413.

46 S. Ayyappan, J. Philip and B. Raj, A facile method to control the size and magnetic properties of $CoFe_2O_4$ nanoparticles, *Mater. Chem. Phys.*, 2009, **115**, 712–717.

47 L. Wu, Z. Sun, Y. Zhen, S. Zhu, C. Yang, J. Lu, Y. Tian, D. Zhong and J. Ma, Oxygen Vacancy-Induced Nonradical Degradation of Organics: Critical Trigger of Oxygen (O(2)) in the Fe-Co LDH/Peroxymonosulfate System, *Environ. Sci. Technol.*, 2021, **55**, 15400–15411.

48 A. A. Al-Kahtani and M. F. Abou Taleb, Photocatalytic degradation of Maxilon C.I. basic dye using CS/$CoFe_2O_4$/

GONCs as a heterogeneous photo-Fenton catalyst prepared by gamma irradiation, *J. Hazard. Mater.*, 2016, **309**, 10–19.

49 N. K. Gupta, Y. Ghaffari, S. Kim, J. Bae, K. S. Kim and M. Saifuddin, Photocatalytic Degradation of Organic Pollutants over MFe_2O_4 (M = Co, Ni, Cu, Zn) Nanoparticles at Neutral pH, *Sci. Rep.*, 2020, **10**, 4942.

50 L. Kong, G. Fang, X. Xi, Y. Wen, Y. Chen, M. Xie, F. Zhu, D. Zhou and J. Zhan, A novel peroxymonosulfate activation process by periclase for efficient singlet oxygen-mediated degradation of organic pollutants, *Chem. Eng. J.*, 2021, **403**, 126445.

51 L. Jing, Y. Xu, S. Huang, M. Xie, M. He, H. Xu, H. Li and Q. Zhang, Novel magnetic $CoFe_2O_4$/Ag/Ag_3VO_4 composites: Highly efficient visible light photocatalytic and antibacterial activity, *Appl. Catal., B*, 2016, **199**, 11–22.

52 Y. Sun, Y. Li, S. You, X. Li, Y. Zhang, Z. Cai, M. Liu, N. Ren and J. Zou, Fe_3C/$CoFe_2O_4$ nanoparticles wrapped in one-dimensional MIL-53(Fe)-derived carbon nanofibers as efficient dual-function oxygen catalysts, *Chem. Eng. J.*, 2021, **424**, 130460.

53 X. Wang, Z. Li, Y. Zhang, Q. Li, H. Du, F. Liu, X. Zhang, H. Mu and J. Duan, Enhanced photocatalytic antibacterial and degradation performance by p-n-p type $CoFe_2O_4$/$CoFe_2S_4$/$MgBi_2O_6$ photocatalyst under visible light irradiation, *Chem. Eng. J.*, 2022, **429**, 132270.

54 W. Li, L. C. Bradley and J. J. Watkins, Copolymer Solid-State Electrolytes for 3D Microbatteries via Initiated Chemical Vapor Deposition, *ACS Appl. Mater. Interfaces*, 2019, **11**, 5668–5674.

55 X. Yang, W. Guo and Q. Shen, Formation of disinfection byproducts from chlor(am)ination of algal organic matter, *J. Hazard. Mater.*, 2011, **197**, 378–388.

56 J. C. Sin, S. M. Lam, H. Zeng, H. Lin, H. Li, L. Huang, K. O. Tham, A. R. Mohamed and J. W. Lim, Enhanced synchronous photocatalytic 4-chlorophenol degradation and Cr(VI) reduction by novel magnetic separable visible-light-driven Z-scheme $CoFe_2O_4$/P-doped BiOBr heterojunction nanocomposites, *Environ. Res.*, 2022, **212**, 113394.

57 A. Hassani, P. Eghbali, F. Mahdipour, S. Wacławek, K.-Y. A. Lin and F. Ghanbari, Insights into the synergistic role of photocatalytic activation of peroxymonosulfate by UVA-LED irradiation over $CoFe_2O_4$-rGO nanocomposite towards effective Bisphenol A degradation: Performance, mineralization, and activation mechanism, *Chem. Eng. J.*, 2023, **453**, 139556.

58 M. Srinivas, Preparation, characterization and photocatalytic activity of nickel-substituted $CoFe_2O_4$: exploration of changes in the micro structural parameters and distribution of cations in the lattice, *Mater. Res. Express*, 2019, **6**, 1150f9.

59 G. Zeng, R. Yang, Z. Zhou, J. Huang, M. Danish and S. Lyu, Insights into naphthalene degradation in aqueous solution and soil slurry medium: Performance and mechanisms, *Chemosphere*, 2022, **291**, 132761.

60 N. Olfatmehr, B. Kakavandi and S. M. Khezri, Peroxydisulfate activation by enhanced catalytic activity of $CoFe_2O_4$ anchored on activated carbon: A new sulfate radical-based oxidation study on the Cefixime degradation, *Sep. Purif. Technol.*, 2022, **302**, 121991.

61 L. Wang, N. Kang, L. Gong, C. Wang, K. Yu, C. Wang and B. Zhou, A novel core-shell structured hybrid composed of zinc homobenzotrizoate and silver borotungstate with supercapacitor and photocatalytic dye degradation performance, *J. Energy Storage*, 2022, **46**, 103873.

